Dynamic Antenna Array Design for Scene Classification Through Fourier-Domain Filtering

Daniel Chen, *Graduate Student Member, IEEE*, Stavros Vakalis, *Graduate Student Member, IEEE*, and Jeffrey A. Nanzer, *Senior Member, IEEE*

***Abstract*— We present a new approach to the classification of scenes in the microwave and millimeter-wave bands that leverages a novel dynamic antenna array concept to capture distinct features in the spatial frequency information of the scene. The spatial frequency information of a scene is obtained through its Fourier transform, and by sampling a subset of this information, key features can be extracted and used for image classification. We demonstrate that a dynamic antenna array can synthesize spatial frequency filters, and that scene classification can be accomplished using the filtered signals without full image reconstruction. We develop a new dynamic antenna array concept using only two antennas to generate a ring-shaped spatial frequency filter and explore the use of this concept for the classification of ground scenes. Natural ground scenes tend to have smoother spatial frequency signals, while, in contrast, features such as buildings and roadways result in sharp broadband spatial frequency responses. Using this design, we demonstrate the ability to classify between two classes of ground scenes: those with man-made structures (buildings, roads, etc.) and those without (natural scenes). We demonstrate the ability of the spatial filters synthesized by the proposed dynamic antenna array to achieve a classification accuracy of 0.971 with an empirical true positive rate of 0.982. The method is broadly applicable to microwave and millimeter-wave sensing at any range.**

***Index Terms*— Classification, interferometric imaging, microwave imaging, radar imaging, sparse arrays, spatial frequency.**

I. Introduction

CLASSIFICATION of scenes and images is important for a broad range of commercial, industrial, and scientific applications. Such images are obtained through various sensing mechanisms, most of them being electromagnetic imaging systems [1], [2]. Among the potential frequency bands, microwave and millimeter-wave frequencies are often utilized for sensing. Signals in the microwave and millimeter-wave frequency bands can easily penetrate through smoke, fog, clothing, and many building materials to detect objects, whereas signals in optical and infrared wavelengths are significantly attenuated when propagating through these media [3], [4]. These aspects have contributed to the growing interest in using microwave and millimeter-wave systems for imaging [5], [6] and remote sensing [7]–[9]. For numerous sensing applications, including sensing of the Earth surface from aerial vehicles, or remote imaging of people for security purposes, differentiating between natural and man-made objects is of critical importance [10]–[14].

Differentiation of objects in a scene is typically accomplished through image classification, which requires measurement of the scene, processing to form an image, and processing to classify the image information. All of these stages can be costly in terms of hardware and computational complexity. Images also often contain redundant information, leading to unnecessary collection and processing of redundant data. Both aspects lead to designs with measurements (both hardware and measurement time) and processing that are unnecessary, leading to greater system complexity and cost. Recent developments in computational microwave imaging have shown the potential for reducing hardware requirements by using, e.g., metasurface apertures, while also keeping the data acquisition time shorter than scanning techniques [15], [16]. However, such systems trade these benefits for greatly increased computational cost, as image reconstruction involves solving an inverse problem [17]. Furthermore, computational imaging approaches require exact knowledge of the transmitted signal across space and time, which can be restricting for many applications. Hardware burdens can also be reduced by using interferometric imaging techniques, which eliminates electrical and/or mechanical scanning by realizing larger synthesized apertures with comparably fewer antenna elements to those of traditional phased arrays and/or focal-plane arrays [18]–[24]. Interferometric imaging samples information in the spatial frequency domain, or Fourier domain of the scene, and relies only on Fourier transforms for image reconstruction, greatly reducing the computational burden compared to other computational imaging approaches.

We propose a new dynamic antenna array concept that uses rotational spatiotemporal dynamics to measure filtered Fourier-domain information that can be used to classify scenes, without full image reconstruction, using only two antennas. The dynamic motion of the antennas creates a spatial frequency filter that captures the features particular to man-made shapes in scenes, and can thus support differentiation between natural and man-made objects in scenes without processing full image data, and with significantly less hardware than current imaging approaches. Previously, we investigated the features presented in the spatial frequency domain captured

Manuscript received July 8, 2020; revised January 15, 2021; accepted January 24, 2021. Date of publication April 5, 2021; date of current version September 3, 2021. This work was supported in part by the National Science Foundation under Grant 1751655. *(Corresponding author: Jeffrey A. Nanzer.)*

The authors are with the Electrical and Computer Engineering Department, Michigan State University, East Lansing, MI 48824 USA (e-mail: chendan7@msu.edu; vakaliss@msu.edu; nanzer@msu.edu).

Color versions of one or more figures in this article are available at https://doi.org/10.1109/TAP.2021.3069521.

Digital Object Identifier 10.1109/TAP.2021.3069521

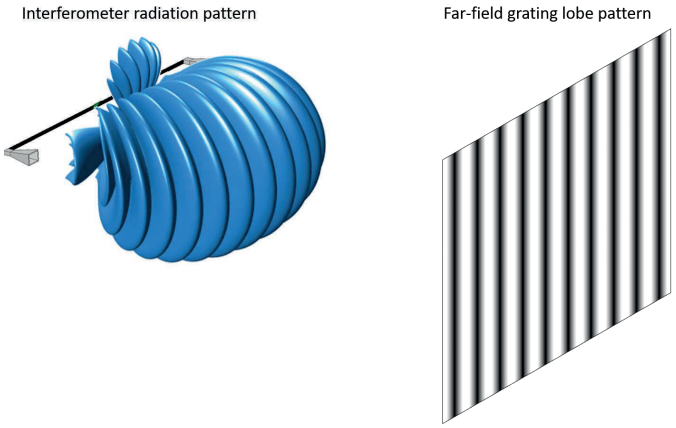

Fig. 1. Interferometer radiation pattern and projected pattern in the far-field. The sinusoidal pattern maps to a specific spatial frequency.

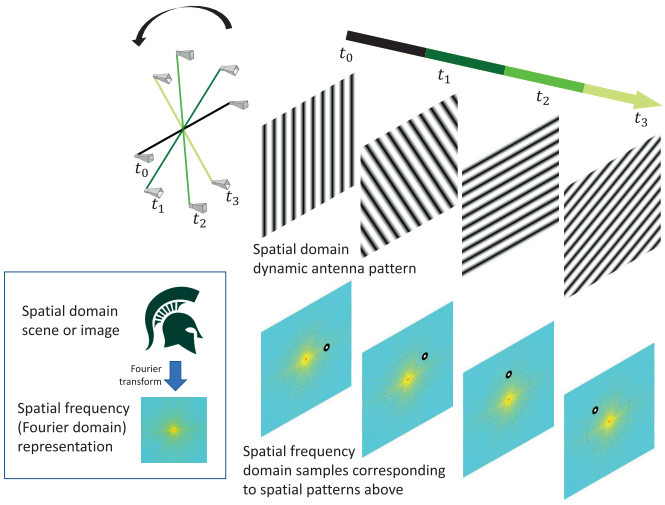

Fig. 2. As the two-element dynamic antenna array rotates, the measured spatial frequency also rotates. This is demonstrated with four different time instances where t_0 corresponds to initial position, t_1 corresponds to 30°, t_2 corresponds to 90°, and t_3 corresponds to 120° counterclockwise rotation from the initial position.

by a ring-shaped sampling function [25]; here, we propose a dynamic array implementation and investigate its use in ground scene classification. In addition to using far less hardware, when implemented with fast dynamics the proposed method can alleviate challenges that are encountered in other sensing modalities like synthetic aperture radar (SAR) imaging, such as blurring due to moving objects on the ground. We explore the use of filtered Fourier-domain image classification on existing sets of measured microwave radar imagery, demonstrating the ability to classify scenes that include man-made structures (buildings, roads, etc.) and scenes that are natural (e.g., forests) using a notional millimeter-wave two-element sensing system. Beyond remote sensing, the concept can be applied more broadly to applications including contraband detection and other short-range sensing applications.

This article is organized as follows. In Section II, the dynamic array scene classification concept is described in more detail, along with a discussion on Fourier-domain image formation and the unique spatial frequency domain features that manifest from different spatial domain scenes. The design of dynamic antenna arrays for spatial frequency domain filtering is presented in Section III, along with a discussion of spatial frequency filter design considerations. Specific sampling functions in the spatial frequency domain are proposed, and we present millimeter-wave antenna designs amenable to implementation on aerial platforms with rotating blades. In Section IV, we present a classification analysis based on the array designed in Section III operating on a set of radar images of ground scenes. We demonstrate the ability to classify natural scenes and scenes with man-made structures such as roads and buildings with high accuracy, demonstrating the capability of a dynamic antenna array to classify scenes without the need for image reconstruction.

II. Image Reconstruction and Spatial Frequency Domain Features in Fourier-Domain Imaging

Interferometric imaging is a sparse array technique that was initially developed as an alternative to real aperture measurements for achieving high-resolution imagery in radio astronomy and remote sensing [18], [26]. Signals are received at multiple antennas and cross-correlated to generate samples of the Fourier-domain information. As shown in Fig. 1, an interferometric antenna pair generates a grating lobe pattern that matches to a specific spatial frequency in the far-field. Antenna array apertures can thus be designed to capture specific spatial frequencies of interest, a key concept in our dynamic antenna array approach. The signals received by the interferometer may be intrinsically generated by the scene, as is the case in passive imagers, or actively transmitted by the imaging system if the transmitted signals are spatiotemporally uncorrelated. Both passive [26]–[29] and active [30]–[32] interferometric techniques have been implemented in various applications ranging from space-borne remote sensors to contraband detection.

The proposed approach to microwave and millimeter-wave scene classification combines interferometric imaging and a novel dynamic antenna array concept to sample sparse Fourier-domain information through dynamic spatiotemporal modulation using only two antenna elements, providing scene classification with only two antenna elements. The concept is shown in Fig. 2. As the dynamic array rotates, the interference pattern corresponding to a specific spatial frequency sample rotates in the Fourier (spatial frequency) domain. The ring-shaped filter produced by the dynamic rotation can thus capture unique features in the spatial frequency spectrum. The dynamic antenna array is a key component of the concept and is designed to generate a specific spatial frequency filter to select key features in the spatial frequency domain that can be used for image classification, without actually reconstructing the entire image, thus leading to a lower hardware burden. Furthermore, the spatial frequency samples are obtained through Fourier transform, leading to low computational complexity.

A. Interferometric Fourier-Domain Imaging

Interferometric imagers sample the scene in the Fourier transform domain of the scene intensity, yielding information

in the spatial frequency domain, which is referred to as the *visibility* $V(u, v)$, where u and v correspond to the two spatial frequency dimensions. The visibility is the 2-D Fourier transform of the spatial scene intensity $I(\alpha, \beta)$ where α and β represent the direction cosines, defined as $\alpha = \sin\theta\cos\phi$ and $\beta = \sin\theta\sin\phi$. The intensity is proportional to the power of the signals from the scene, which may be intrinsically generated in the scene by thermal means [33] or may be representative of a reflected signal from an active transmitter [30]. The relationship between visibility and spatial scene intensity is given by

$$V(u, v) = \int_{-\infty}^{\infty}\int_{-\infty}^{\infty} I(\alpha, \beta)e^{j2\pi(u\alpha+v\beta)}d\alpha d\beta. \quad (1)$$

Once the visibility is measured, the reconstructed scene intensity is then given by

$$I_r(\alpha, \beta) = \int_{-\infty}^{\infty}\int_{-\infty}^{\infty} V(u, v)S(u, v)e^{-j2\pi(u\alpha+v\beta)}dudv. \quad (2)$$

In practice, the visibility is typically sampled discretely, as opposed to the continuous formulation above. With a sparse array of antenna elements, the cross correlation of the received signals at an antenna pair with baseline separation D represents a sample of the visibility. Providing the received radiation is spatially and temporally incoherent, a sufficient number of visibility samples will then enable image reconstruction through inverse Fourier transform, per the Van Cittert-Zernike theorem [34], albeit with the requisite sampling theorem nonidealities such as spatial ambiguities. The complete set of all acquired discrete 2-D spatial frequencies is referred to as the *sampling function* which is given by

$$S(u, v) = \sum_{n}^{N}\sum_{m}^{M}\delta(u - u_n)\delta(v - v_m), \quad (3)$$

where the product of N and M denotes the maximum number of spatial frequencies that the receiving array can acquire. The sampled visibility $V_s(u, v) = V(u, v) \cdot S(u, v)$ is the product between the scene visibility and the sampling function, from which the reconstructed image I_r can be found by

$$I_r(\alpha, \beta) = \sum_{n}^{N}\sum_{m}^{M} V(u_n, v_m)e^{-j2\pi(u_n\alpha+v_m\beta)}. \quad (4)$$

Typically, the reconstructed image intensity I_r is then inputted into a classification algorithm. In contrast, here we explore the potential for image classification using only the sampled visibility V_s, without full image reconstruction. In particular, we are interested in the potential for scene classification with a minimal subset of information in the spatial frequency domain that can be efficiently sampled with a dynamic antenna array. While interferometric arrays use far fewer antenna elements than traditional phased arrays, appropriately designing array dynamics can further reduce hardware requirements by dynamically moving antennas to synthesize a larger physical array over time. This aspect is exploited in radio astronomy arrays, where the rotation of the Earth is leveraged to change the apparent baselines relative to a given celestial direction, over time filling in a more dense sampling function than the array obtains statically [18]. However, Earth rotation dynamics are slow, and nonetheless inapplicable outside of astronomical observation. In contrast, recent work by the authors has demonstrated the capabilities of relatively faster platform dynamics in distributed arrays to improve array performance, such as reducing radiation pattern sidelobes [35], [36]. Furthermore, the rotation concept has also been used in imaging techniques using linear arrays and Radon transform-based tomographic reconstruction [37].

B. Scene-Related Features in the Fourier Domain

To explore the feasibility of filtered Fourier-domain image classification, we consider aerial images of ground scenes obtained with microwave radar, to classify between natural scenes (NSs) with no man-made structures, and non-natural scenes (NNSs) containing man-made structures such as buildings and/or roadways. The proposed application is applicable to a broader set of microwave and millimeter-wave applications; however, we choose microwave ground images for the following reasons: First, large data sets of ground scenes captured with SAR are available, providing enough data to perform rigorous statistical classification analysis of the proposed filtered Fourier-domain classification approach; in this work we selected radar images from [38] which have been processed to establish a common resolution of 1 m/pixel. Second, the approach is proposed for implementation at millimeter-wave frequencies, and microwave radar ground images provide resolutions and reflectivity closer to the ones obtained at low millimeter-wave frequencies (e.g. 40 GHz) than optical or infrared images. Finally, a practical system implementation of a 40 GHz two-element antenna array with spatiotemporal dynamics providing image resolution and field-of-view commensurate with the chosen data set is explored for ground-based scene classification; the proposed system could be implemented in passive or active interferometric modes. We note that while the use of measured SAR data sets may not provide a precise model of the proposed implementation, we contend that the presented approach is the most reasonable for exploring the feasibility of the proposed sparse Fourier-domain scene classification method.

Sparse Fourier-domain scene classification is based on the prominence of spatial frequency domain features that are present in NNSs and absent in NSs. In particular, scenes with sharp edges, common with man-made objects but infrequent in NSs, generate strong discrete directional signals in the spatial frequency domain, while such discrete directional components are generally absent in NSs. We consider examples of a NS image represented by region of vegetation and a NNS image represented by highway and building clusters that have a spatial field of view of 1000 m $\times$ 1000 m in Fig. 3(a) and (b) together with their corresponding visibility in Fig. 3(c) and (d). The NS visibility shows smoother spatial frequency content, while the NNS visibility presents strong discrete directional components; these signals are oriented orthogonal to the direction of sharp edges in the spatial domain scene. The fact that these signals manifest in discrete and highly directional

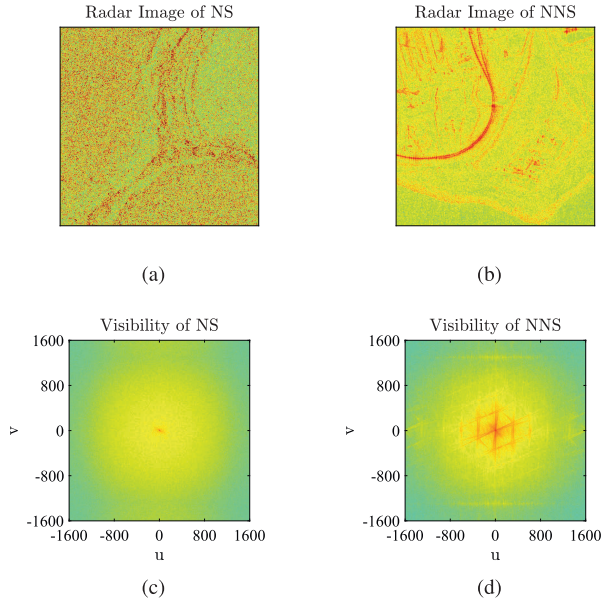

Fig. 3. Microwave radar images of (a) a natural scene (NS) of a vegetation region of Campo Grande, Brazil and (b) a non-natural scene (NNS) of highway and building cluster from region of Port Hedland, Western Australia with their corresponding visibility in (c) and (d), respectively (data from [38]).

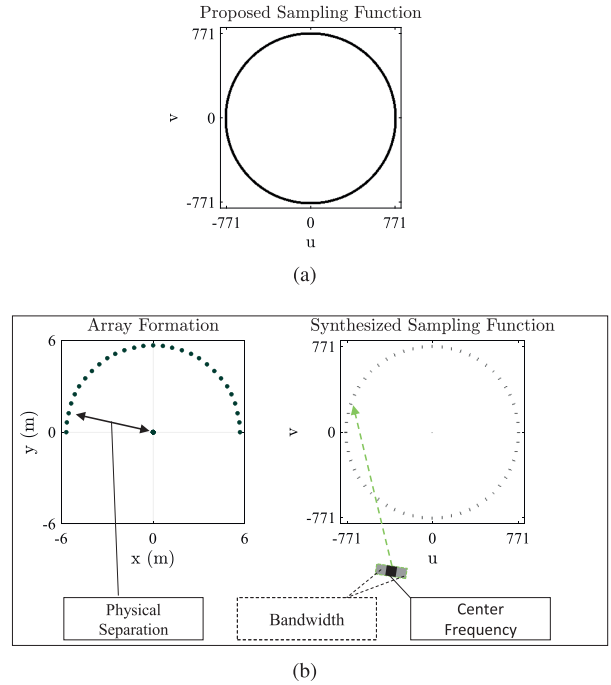

Fig. 4. (a) Proposed ring-shaped sampling function. (b) Discrete array formation of 30 antennas (left) and its corresponding discrete synthesized ring-shaped sampling function (right). The double arrow annotation on the array formation denotes the physical separation or baseline between the two antennas. The corresponding portion of the resulting sampling function is annotated by the green arrow. The thickness of the ring-shaped sampling function on the uv-plane comes from both the center frequency and the bandwidth of antennas and is denoted by solid and dashed lines, respectively.

orientations enables relatively simple methods of detection based on only a small subset of visibility data. In the next section, we describe the design of a dynamic antenna array to sample the visibility in a ring in the u-v domain at a given radius, providing detectability of the discrete changes in visibility as a function of spatial frequency domain angle present in NNS data and absent in NS data.

III. Dynamic Antenna Array Design for Sparse Fourier-Domain Sampling

A visibility sample is obtained by cross-correlating the received signals captured by two antennas separated by a baseline D. In the two-dimensional (2-D) Fourier space, the 2-D spatial frequency at which the visibility is captured is given by the separations in the x and y dimensions, i.e., $u = D_x/\lambda$ rad^{-1} and $v = D_y/\lambda$ rad^{-1}. The spatial frequency of a 2-D array sampling function can thus be populated by designing a static set of multiple antennas, the outputs of which are cross-correlated pairwise; by using only two antennas and dynamically moving one or both to build up the sampling function over time; or a combination of the two. In contrast to traditional interferometric imaging approaches, in this work we are interested in sampling only a specific subset of the Fourier-domain information, in particular a subset that enables the detection of the directional components manifesting from sharp edges in the image. This can be accomplished most effectively with a ring-shaped sampling function [39], as shown in Fig. 4(a).

A ring-shaped sampling function can be obtained by placing an antenna at the center of a semicircle with additional antennas throughout the arc of the same semicircle where the radius is the physical separation matching the center spatial frequency of the spatial-spectral bandwidth of the ring filter. By implementing cross correlation between the ring elements and the center element, a sample of the ring-shaped sampling function can be obtained. However, this sampling function only collects information at discrete spatial frequencies; spatial bandwidth can be added to the sampling function by imparting a (temporal) frequency bandwidth on the receiver system. Since the spatial frequency is defined in terms of both the antenna separation and the wavelength, adding bandwidth effectively modulates the spatial frequency at which the information is captured. This conceptual array formation and its corresponding sampling function are shown in Fig. 4(b). Each segment within the sampling function includes the contribution due to physical separation/center frequency, and the temporal bandwidth. As observed, the median radius of the sampling function is dependent on the physical separation and the center frequency and the effective spatial bandwidth of the ring is proportional to the frequency bandwidth. We note that since the 2-D spatial frequency domain is conjugate symmetric for image intensities, which have real amplitudes, sampling is only required to be implemented over half of the spatial domain. This also implies that the angular position of ϕ in the spatial domain corresponds to both ϕ and $\phi + 180°$ of the ring-shaped sampling function being formed in the spatial frequency domain, thus a 180° rotation between the two antennas will yield a full circle of the proposed ring-shaped sampling function. Thus, the effective sampling function can

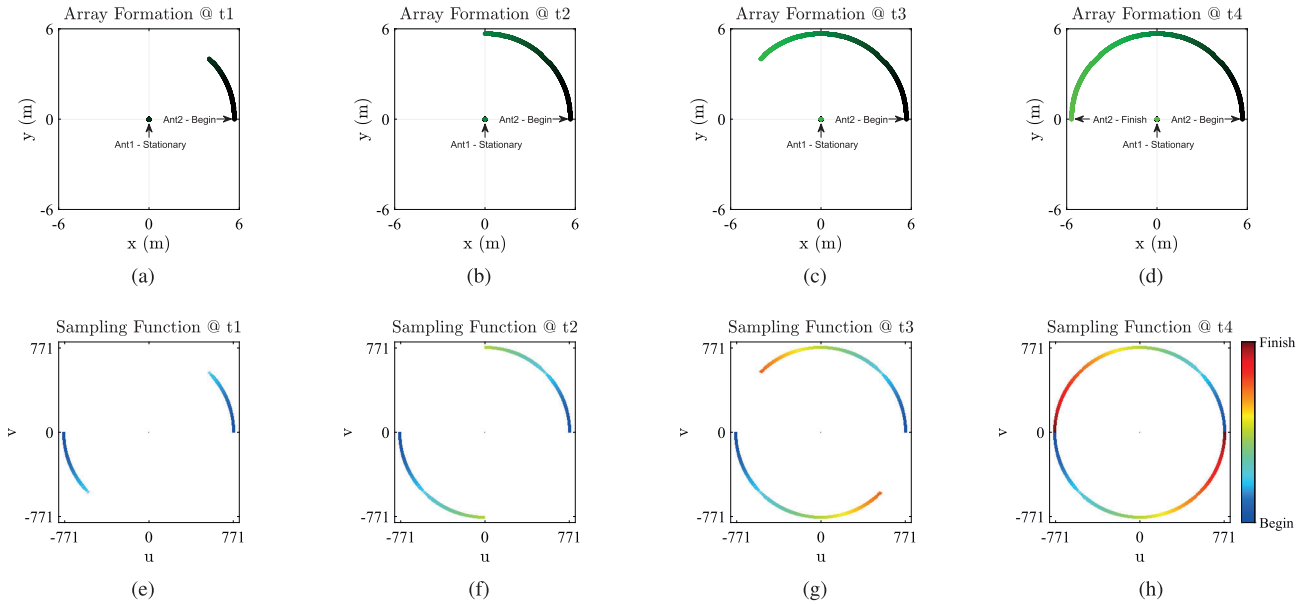

Fig. 5. Formation of the sampling function using two antennas with the first element fixed at the center of a semicircle and the second element moving along the semicircular path. (a)–(d) Representation of the elapsed array formations over a full semicircular path at four different times with (e)–(h) representing the corresponding elapsed sampling functions.

be represented by

$$S_{Ring}(u,v) = \sum_{\phi=\phi_0}^{\phi_0+180^\circ} \delta(u - D_\lambda \cos\phi)\delta(v - D_\lambda \sin\phi), \quad (5)$$

where D_λ is the separation between the two antennas, ϕ is the rotation angle, and ϕ_0 is a nominal initial angle.

A. Spatial Frequency Filter Design Considerations

The design of the spatial frequency bandwidth of the ring filter will, in general, depend on the application. The filter should be selected within a region where discrete, broadband spatial-spectral signals have good signal strength compared to the surrounding visibility data. Typical scenes contain a significant amount of information at low spatial frequencies, resulting in strong visibility content near $(u = 0, v = 0)$, as can be seen in Fig. 3(c), thus it is beneficial to generate the ring filter with a radius beyond the strong low-frequency content, but sufficiently close-in that the strong discrete signals are not low in signal strength. In the application example in this article, the visibility data in Fig. 3(d) suggests a ring filter covering a spatial spectral bandwidth near 700–800 rad^{-1}. We determined heuristically that the discrete spectral signals have a good signal strength compared to the surrounding visibility near 761 rad^{-1}, as discussed in the following dynamic antenna design. Applications with different scenes will result in different visibility distributions; as such, the spatial-spectral bandwidth of the ring filter, and the dynamic antenna frequency and baseline, may need to be designed for the specific application.

Implementing a ring-shaped sampling function with a stationary array requires the use of fewer antenna elements than a traditional phased array imaging system; however, the number of elements necessary can be further reduced by a significant margin through array dynamics. By moving antennas in space, a range of spatial frequencies can be implemented with only a few elements, as shown in Fig. 5 where the progression of an antenna moving in an arc and the corresponding sampling function at specific instances of the rotation period are shown. It can be seen that a counterclockwise rotational movement on the xy-plane corresponds to counterclockwise rotational course on the uv-plane. Since this particular concept uses one stationary element and one dynamic element, co-polarization must be maintained, for which circularly polarized antennas could be implemented [40], [41]. This concept requires no reset of the position, i.e. continuing rotation on the complementing semicircular path will generate the same sampling function thus each successful revolution of the dynamic array corresponds to two revolutions of the dynamic sampling function. Building on this dynamic movement concept, a simple dynamic array can be designed with two elements on a rotating platform, as shown in Fig. 6. Two antenna elements located on, for example, the rotor blades of a vehicle, would provide sufficient spatial coverage for the desired ring-shaped sampling function. The construction of the sampling function using such a dynamic antenna array is shown in Fig. 7. In such

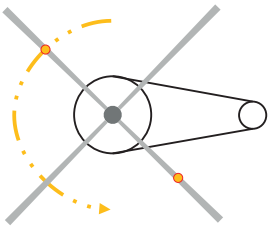

Fig. 6. Illustration of a notional dynamic array implementation using the concept shown in Fig. 7 on a platform with rotors.

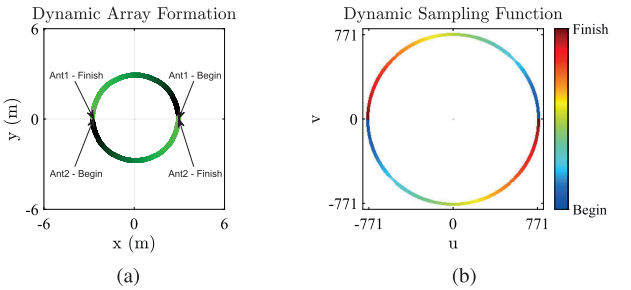

Fig. 7. Array dynamics and sampling function formation of the implementation in Fig. 6. (a) Dynamic array formation due to the movement of two antennas. (b) Corresponding elapsed sampling function.

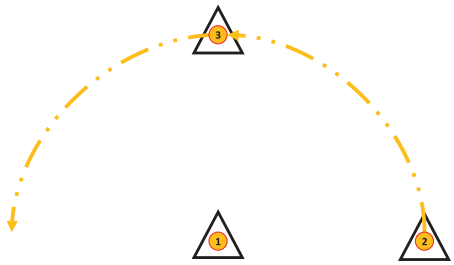

Fig. 8. Illustration of a multi-platform concept to acquire the sampling function shown in Fig. 4(a). Each platform noted by 1, 2, and 3 consists of one integrated antenna. Platform 1 holds stationary, while 2 and 3 move around the segmented semicircular path with respect to platform 1.

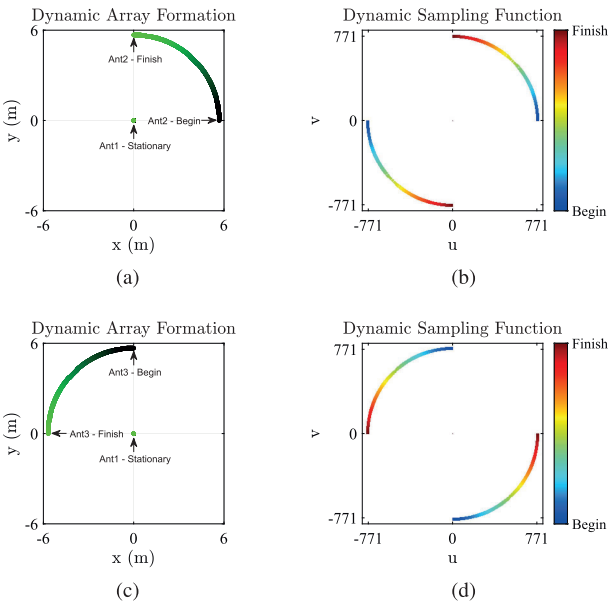

Fig. 9. Formation of the sampling function with three antennas integrated separately on three platforms as shown in Fig. 8. (a) Dynamic array formation with counterclockwise platform (Ant2) movement in the first quadrant on the xy-plane and (b) corresponding dynamic sampling function formed in counterclockwise direction in the first and third quadrant on the uv-plane. (c) Dynamic array formation with counterclockwise platform (Ant3) movement in the second quadrant on the xy-plane and, (d) the corresponding dynamic sampling function formed in counterclockwise direction in the second and fourth quadrant on the uv-plane.

a configuration the antennas remain co-polarized, enabling appropriate sampling of the received signals in either active or passive interferometric imaging approaches as described earlier. Such an implementation can also be achieved on platforms with fast enough rotations to support imaging while in motion.

Multi-platform concepts are also feasible. Prior work has shown the potential for multi-platform distributed array concepts to mitigate sidelobes [35], [36], and the ability to wirelessly coordinate the operations of sensors on distributed platforms is becoming increasingly feasible [42]–[44]. Three separate platforms moving dynamically relative to one another can be used to obtain the ring-shaped sampling function that leverages the relative motions from multiple platforms. This can be accomplished with one stationary platform and a second platform that moves along the semicircular path with respect to the stationary platform (Fig. 5); a three platform concept (Fig. 8) has the potential to acquire the same sampling function in half the time. While platform 1 in Fig. 8 is holding stationary, platform 2 and 3 each complete half of the semicircular path as shown in Fig. 9(a) and (c) that will generate the corresponding sampling function as shown in Fig. 9(b) and (d), respectively.

B. 40 GHz Dynamic Array Design on Rotating Blades

We refine the two-element dynamic array concept by considering a millimeter-wave array amenable to implementation on the rotors of a small aerial vehicle. We consider a center frequency of 40 GHz, a bandwidth of 3%, and antennas with a half-power beamwidth θ_{BW} of 60°, commensurate with the beamwidth of a planar patch antenna that could reasonably be implemented conformally on the underside of the rotors [45]–[47]. While considerations must be made to obtain the desired signal-to-noise ratio (SNR), recent developments in active interferometric imaging lend feasibility to achieving an appropriate SNR [30], [31]. Given the above parameters, we consider a design procedure that balances feasible antenna separation and platform altitude to maintain a ground resolution of 1 m, which is commensurate with the resolution of the analyzed data set from [38] (although the radar data in [38] was measured at X-band, the common image resolution of 1 m in the data and the proposed design supports a feasible comparison).

For a single antenna system, the one-dimensional (1-D) spatial resolution, $\Delta\theta$, can be expressed in terms of the antenna beamwidth as

$$\Delta\theta = \frac{\tan(\theta_{BW})}{R}, \tag{6}$$

where R is the distance between the antenna and point of interest, which is the altitude in the present analysis. For a two-element sparse or distributed array, the spatial resolution is governed by its maximum antenna baseline D_{max} and wavelength λ using [3]

$$\Delta\theta \approx 0.88 \cdot \frac{\lambda}{D_{max}}. \tag{7}$$

The relationships between altitude, baseline and antenna beamwidth is shown in Fig. 10, obtained from applying (6) and (7). Using the stated assumptions above, the calculated altitude is approximately 886 m, the calculated baseline

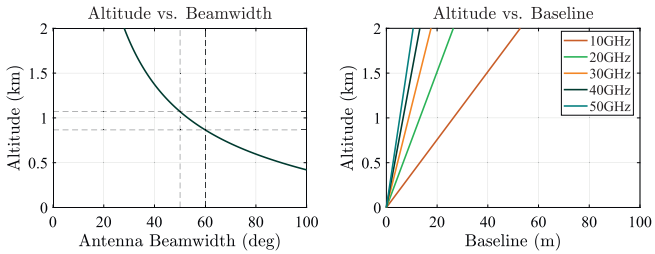

(a) (b)

Fig. 10. (a) Calculated altitude versus antenna beamwidth, with markers indicating beamwidth values between 50° and 60°, matching that of a feasible patch antenna. (b) Calculated altitude versus maximum system baseline for center frequency of 10, 20, 30, 40, and 50 GHz.

TABLE I
DYNAMIC ARRAY DESIGN PARAMETERS

Bandwidth	Frequency	Wavelength	Baseline
−1.5%	39.4 GHz	7.6 mm	751 λ
±0%	40.0 GHz	7.5 mm	761 λ
+1.5%	40.6 GHz	7.4 mm	771 λ

is approximately 761 λ (equivalent to 761 rad^{-1} in the spatial frequency domain), which translates to a physical separation of 5.7 m. For a single platform implementation, the calculated altitude and required physical separation match the typical specification of a medium-sized unmanned aerial vehicle (UAV) as discussed in [48] where the average end to end rotor blade length or wingspan is 5–10 m. The proposed concept is thus amenable to being implemented on research/industrial-grade UAV helicopters such as the StarLite-2A [49]. With a physical separation fixed at 5.7 m, the 3% bandwidth of the antenna will contribute to a range of baselines approximately between 751 λ and 771 λ (see Table I).

IV. ANALYSIS OF GROUND SCENE CLASSIFICATION USING DYNAMIC ARRAY SPATIAL FREQUENCY FILTER

We explore the application of the spatial frequency ring filter to the classification of ground scenes. The objective is to demonstrate the ability to classify between NSs, which lack strong broad spatial spectral responses [Fig. 3(c)], and NNSs including man-made structures that generate such features [Fig. 3(d)]. In doing so, we demonstrate that the broad spatial spectral responses of man-made objects are sufficiently persistent in a large set of real data that a dynamic antenna array can be designed that captures such information for direct classification. We calculate a 1-D signal that is the average of the sampled visibility at every rotation angle within the output of the ring filter, providing a measure of the intensity of the radial spatial frequency within the filter bandwidth as a function of angle in the uv-plane. Generally, NS images demonstrate fewer variations as a function of angle than NNS images. The data set described in Section II was divided into training and evaluation subsets. Standard metrics were calculated based on a set of statistical measures of the resultant signals from the training subset. These metrics are used to determine features that provide reasonable separation between the probability distributions of the two classes; the larger the separation, the better the potential for classification. From a set of the most prominent features we determined analytical threshold values. As a comparison, these thresholds are compared to an "ideal" threshold calculated empirically by evaluating all thresholds over the entire data set.

To evaluate the performance of the proposed classification objectives, we evaluate a standard set of metrics, including the true positive rate (TPR), which indicates actual positives that are correctly identified; the true negative rate (TNR), which indicates actual negatives that are correctly identified; the positive predictive value (PPV), which indicates actual positives in proportion to all identified positives; the negative predictive value (NPV), which indicates actual negatives in proportion to all identified negatives; the accuracy (ACC), which provides insight to the measure of all the correctly identified cases; and the F1 Score (F1), which is the harmonic mean between PPV and TPR that gives a better measure of the incorrectly classified cases than ACC [50], [51].

The proposed classification method depends on deriving useful statistics from the sampled visibility after applying the ring-shaped sampling function. The filtered spatial frequencies can be transformed to a 1-D vector S_s by calculating the average response at each angle that spans the complete 360° with respect to the center of the uv-plane, given by

$$S_s(\gamma) = \frac{\sum_{r=M}^{N} V_s(r\cos(\gamma), r\sin(\gamma))}{N-M}, \tag{8}$$

where γ represents the angle with respect to the positive u-axis, V_s represents the sampled visibility, r represents the radius of the ring-shaped sampling function, N represents the distance between the furthest uv pair sampled from the center of the uv-plane which is due to the antenna's upper bandwidth limit; and M represents the distance between the closest uv pair sampled from the center of the uv-plane which is due to the antenna's lower bandwidth limit. An example of S_s is shown in Fig. 11(a). While apparent differences in S_s can exist between of NS and NNS, the first derivative of the ring-filtered sampled visibility

$$S_s'(\gamma) = \frac{d}{d\gamma} S_s(\gamma) \tag{9}$$

an example of which is shown in Fig. 11(b), is preferable for two reasons: the first derivative puts more weight on the change of S_s due to the discrete nature of a NNS and less on the smoother responses from a NS; and variations in the magnitude of the responses, which may fluctuate as different regions and/or operating conditions are encountered, are mitigated.

A set of 2076 images from [38], including 1038 NS and 1038 NNS images, were processed with the sampling function based on the dynamic array design and the corresponding $S_s'(\gamma)$ vectors were computed. From these, the mean value as a function of angle

$$\mu S_s' = \text{mean}\{S_s'(\gamma)\} \tag{10}$$

was calculated for each data set. We define a classification threshold based on the maximum and minimum values of all

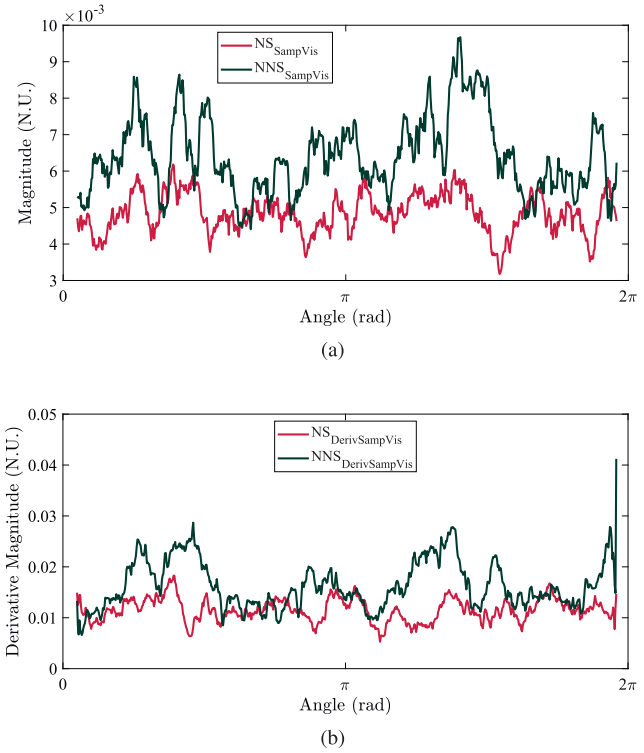

Fig. 11. (a) Visualization of the transformed 1-D sampled visibility vector (S_s) of NS and NNS from Fig. 3(a) and (b) by averaging the response at each angle with respect to the center of the uv-plane. (b) Corresponding first derivatives (S_s').

$\mu S_s'$ values from a training set by

$$\mathrm{T} = \frac{1}{2}\left(\max\left\{\mathrm{NS}_{\mu S_s'}\right\} + \min\left\{\mathrm{NNS}_{\mu S_s'}\right\}\right). \tag{11}$$

Scenes from the testing set with $\mu S_s' < \mathrm{T}$ are classified as NS, whereas scenes with $\mu S_s' > \mathrm{T}$ are classified as NNS. To avoid potential bias by unintentionally selecting the best or worst-case scenario as a result of using specific training and testing group combinations, we leverage the Monte Carlo method [52] by repeating the following three steps 1 000 000 times.

1) Of the selected 1038 NS images and 1038 NNS images, 727 images (≈70%) from each image type are uniformly selected at random to form the training group for threshold calculation and the remaining 313 images (≈30%) from each image type form the testing group for classification.
2) The threshold is calculated using the maximum and minimum $\mu S_s'$ values from the training group using (11).
3) The calculated threshold is applied to the testing group for classification and the classification metrics noted previously are calculated.

In practical applications, classifier thresholds are determined as above, using a training and testing set. To compare the threshold above, we determined an ideal threshold value from the full data set. This provides the best possible classification results, but is specifically tuned to the entire data set, and thus is useful mainly for comparison of the analytical threshold above. The range of the threshold is bounded by the lowest and highest value from the computed means of the S_s' vectors which are from the selected 1038 NS images and 1038 NNS images. 1000 equally spaced steps between the upper- and lower-bound are generated and applied to all 2076 images for classification with the classification metrics noted previously recorded. The results are shown in Table II where each column represents the highest achievable value of the specific classification metric with its associated values on other classification metrics and the normalized threshold. For applications requiring guaranteed classification of NNS (i.e. TPR = 1.000), the associated trade off is a lower ACC of 0.667 and F1 of 0.750. Similarly, for applications requiring guaranteed classification of NS (i.e. TNR = 1.000), the outcome will have an associated ACC of 0.961 and F1 of 0.959. Of the various thresholds, a value of 0.163 N.U. provided the best overall performance among the various metrics.

TABLE II
METRIC INTERDEPENDENCY USING EMPIRICAL THRESHOLD

	TPR =1.000	TNR =1.000	PPV =1.000	NPV =1.000	ACC =0.979	F1 =0.979
TPR	-	0.922	0.922	1.000	0.968	0.968
TNR	0.334	-	1.000	0.334	0.990	0.990
PPV	0.600	1.000	-	0.600	0.990	0.990
NPV	1.000	0.928	0.928	-	0.969	0.969
ACC	0.667	0.961	0.961	0.667	-	0.979
F1	0.750	0.959	0.959	0.750	0.979	-
Threshold (N.U.)	0.139	0.177	0.177	0.139	0.163	0.163

TABLE III
CLASSIFICATION RESULTS USING EMPIRICAL AND ANALYTICAL THRESHOLDS

	Empirical Value	Mean Analytical Value	% Error
T (N.U.)	0.163	0.158	3.1
ACC	0.979	0.971	0.9
F1	0.979	0.971	0.8
TPR	0.968	0.982	1.4
TNR	0.990	0.960	3.1
PPV	0.990	0.961	3.0
NPV	0.969	0.981	1.3

Table III presents a comparison of the threshold resulting from the analytical approach and that of the ideal threshold. The mean analytical threshold value of 0.158 N.U. is very close to the ideal threshold value of 0.163 N.U. obtained using the entire data set, indicating that setting the classifier threshold using the analytical approach can be expected to provide close to optimal results. Fig. 12 shows the probability density functions of the two data subsets (NS and NNS) as a function of $\mu S_s'$. There is a clear null point between the distributions, indicating a desirable point at which to choose the threshold. The empirical ideal value, along with the analytical value, closely matches this null point, indicating that the analytical approach can be expected to produce a desirable threshold value. The classification metrics using the analytical threshold are furthermore within 3% of the ideal values. Thus, scene classification is obtained with high classification metrics using only a very sparse set of Fourier-domain scene information.

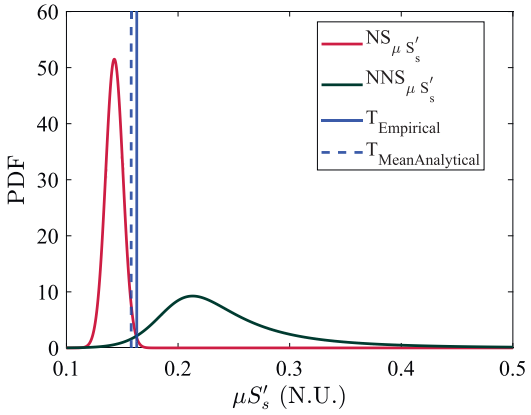

Fig. 12. Probability density function of $NS_{\mu S'_s}$ (shown in red) and $NNS_{\mu S'_s}$ (shown in green) with the empirical and mean analytical threshold value shown in solid- and dashed-blue lines, respectively.

V. Conclusion

In this work, we aim to provide a framework for microwave scene classification based on a small subset of the information captured using a dynamic antenna array. Ring-shaped spatial frequency filters were shown to capture useful spatial frequency domain information that can be used to differentiate between scenes with structured, man-made objects such as roadways and buildings, and those without. Furthermore, through the use of a novel dynamic antenna array concept, the spatial frequency ring filter was shown to be feasible to implement in millimeter-wave hardware with only two receiving antenna elements, enabling information collection with significantly less hardware than typical imaging systems. Classification results were presented for a set of microwave ground images with resolution commensurate with that possible in a millimeter-wave aerial implementation using analytical thresholds. While the presented work used ground scenes as a working example, the overall concept may be applied to microwave and millimeter-wave image classification problems in general.

References

[1] A. Godavarty *et al.*, "Non-invasive optical imaging technology: Breast cancer imaging and functional brain mapping," in *Proc. Pan Amer. Health Care Exchanges*, Mar. 2012, p. 125.

[2] K. Hossain, C. Mantel, and S. Forchhammer, "Evaluation of prediction of quality metrics for IR images for UAV applications," in *Proc. Data Compress. Conf. (DCC)*, Mar. 2019, p. 578.

[3] J. A. Nanzer, *Microwave and Millimeter-Wave Remote Sensing for Security Applications*. Norwood, MA, USA: Artech House, 2012.

[4] N. Currie and C. Brown, *Principles and Applications of Millimeter-Wave Radar*. Norwood, MA, USA: Artech House, 1987.

[5] E. C. Fear, X. Li, S. C. Hagness, and M. A. Stuchly, "Confocal microwave imaging for breast cancer detection: Localization of tumors in three dimensions," *IEEE Trans. Biomed. Eng.*, vol. 49, no. 8, pp. 812–822, Aug. 2002.

[6] D. M. Sheen, D. L. Mcmakin, and T. E. Hall, "Three-dimensional millimeter-wave imaging for concealed weapon detection," *IEEE Trans. Microw. Theory Techn.*, vol. 49, no. 9, pp. 1581–1592, Sep. 2001.

[7] L. C. Graham, "Synthetic interferometer radar for topographic mapping," *Proc. IEEE*, vol. 62, no. 6, pp. 763–768, Jun. 1974.

[8] D. Moller *et al.*, "The glacier and land ice surface topography interferometer: An airborne proof-of-concept demonstration of high-precision Ka-band single-pass elevation mapping," *IEEE Trans. Geosci. Remote Sens.*, vol. 49, no. 2, pp. 827–842, Feb. 2011.

[9] R. Seu, S. Smrekar, S. Hensley, and P. Lombardo, "A SAR interferometer experiment to explore the surface of Venus," in *Proc. 11th Eur. Conf. Synth. Aperture Radar (EUSAR)*, Jun. 2016, pp. 1–3.

[10] J. P. P. Gomes, J. F. B. Brancalion, and D. Fernandes, "Automatic target recognition in synthetic aperture radar image using multiresolution analysis and classifiers combination," in *Proc. IEEE Radar Conf.*, May 2008, pp. 1–5.

[11] U. Srinivas, V. Monga, and R. G. Raj, "SAR automatic target recognition using discriminative graphical models," *IEEE Trans. Aerosp. Electron. Syst.*, vol. 50, no. 1, pp. 591–606, Jan. 2014.

[12] S. Stanko *et al.*, "Active and passive mm-wave imaging for concealed weapon detection and surveillance," in *Proc. 33rd Int. Conf. Infr., Millim. THz Waves*, Sep. 2008, pp. 1–2.

[13] F. Gumbmann and L.-P. Schmidt, "Millimeter-wave imaging with optimized sparse periodic array for short-range applications," *IEEE Trans. Geosci. Remote Sens.*, vol. 49, no. 10, pp. 3629–3638, Oct. 2011.

[14] C. Zheng, X. Yao, A. Hu, and J. Miao, "Initial results of a passive millimeter-wave imager used for concealed weapon detection BHU-2D-U," *Prog. Electromagn. Res. C*, vol. 43, pp. 151–163, Jan. 2013.

[15] M. F. Imani *et al.*, "Review of metasurface antennas for computational microwave imaging," *IEEE Trans. Antennas Propag.*, vol. 68, no. 3, pp. 1860–1875, Mar. 2020.

[16] T. Sleasman *et al.*, "Experimental synthetic aperture radar with dynamic metasurfaces," *IEEE Trans. Antennas Propag.*, vol. 65, no. 12, pp. 6864–6877, Dec. 2017.

[17] L. M. Neira, B. D. Van Veen, and S. C. Hagness, "High-resolution microwave breast imaging using a 3-D inverse scattering algorithm with a variable-strength spatial prior constraint," *IEEE Trans. Antennas Propag.*, vol. 65, no. 11, pp. 6002–6014, Nov. 2017.

[18] A. R. Thompson, J. M. Moran, and G. W. Swenson, *Interferometry and Synthesis in Radio Astronomy*. Hoboken, NJ, USA: Wiley, 2001.

[19] J. A. Nanzer, "Millimeter-wave interferometric imaging sensors," in *Proc. IEEE SENSORS*, Nov. 2013, pp. 1–4.

[20] A. Ferretti, C. Prati, and F. Rocca, "Permanent scatterers in SAR interferometry," *IEEE Trans. Geosci. Remote Sens.*, vol. 39, no. 1, pp. 8–20, Jan. 2001.

[21] K. Schulz, D. Brunner, and M. Boldt, "Comparison of covamcoh and ILU image products for interferometric very high resolution SAR image pairs," in *Proc. IEEE Int. Geosci. Remote Sens. Symp.*, Jul. 2011, pp. 313–315.

[22] Y. Álvarez, Y. Rodriguez-Vaqueiro, B. Gonzalez-Valdes, F. Las-Heras, and A. Garcí-Pino, "Fourier-based imaging for subsampled multistatic arrays," *IEEE Trans. Antennas Propag.*, vol. 64, no. 6, pp. 2557–2562, Jun. 2016.

[23] D.-C. Soncco, C. Barbanson, M. Nikolova, A. Almansa, and Y. Ferrec, "Fast and accurate multiplicative decomposition for fringe removal in interferometric images," *IEEE Trans. Comput. Imag.*, vol. 3, no. 2, pp. 187–201, Jun. 2017.

[24] E. Kpré, C. Decroze, M. Mouhamadou, and T. Fromenteze, "Computational imaging for compressive synthetic aperture interferometric radiometer," *IEEE Trans. Antennas Propag.*, vol. 66, no. 10, pp. 5546–5557, Oct. 2018.

[25] D. Chen, S. Vakalis, V. Holmes, and J. A. Nanzer, "Spatial frequency filter design for interferometric image classification without image reconstruction," in *Proc. IEEE Int. Symp. Antennas Propag. USNC-URSI Radio Sci. Meeting*, Jul. 2020, pp. 23–24.

[26] C. S. Ruf, C. T. Swift, A. B. Tanner, and D. M. L. Vine, "Interferometric synthetic aperture microwave radiometry for the remote sensing of the Earth," *IEEE Trans. Geosci. Remote Sens.*, vol. GRS-26, no. 5, pp. 597–611, Sep. 1988.

[27] K. van 't Klooster, "A few examples of interferometry applications in space-related active and passive remote sensing," in *Proc. 2nd Int. Workshop Ultrawideband Ultrashort Impulse Signals*, 2004, pp. 55–58.

[28] T. Amiot, F. Douchin, E. Thouvenot, J. C. Souyris, and B. Cugny, "The interferometric cartwheel: A multi-purpose formation of passive radar microsatellites," in *Proc. IEEE Int. Geosci. Remote Sens. Symp.*, vol. 1, Jun. 2002, pp. 435–437.

[29] P. Bei and W. Ji, "2-D frequency spectrum features and error analysis for interferometric passive microwave imager," in *Proc. Int. Symp. Microw., Antenna, Propag. EMC Technol. Wireless Commun.*, Aug. 2007, pp. 1454–1457.

[30] S. Vakalis and J. A. Nanzer, "Microwave imaging using noise signals," *IEEE Trans. Microw. Theory Techn.*, vol. 66, no. 12, pp. 5842–5851, Dec. 2018.

[31] S. Vakalis, L. Gong, Y. He, J. Papapolymerou, and J. A. Nanzer, "Experimental demonstration and calibration of a 16-element active incoherent millimeter-wave imaging array," *IEEE Trans. Microw. Theory Techn.*, vol. 68, no. 9, pp. 3804–3813, Sep. 2020.

[32] S. Vakalis, L. Gong, and J. A. Nanzer, "Imaging with WiFi," *IEEE Access*, vol. 7, pp. 28616–28624, 2019.
[33] J. A. Nanzer and R. L. Rogers, "Human presence detection using millimeter-wave radiometry," *IEEE Trans. Microw. Theory Techn.*, vol. 55, no. 12, pp. 2727–2733, Dec. 2007.
[34] M. Born *et al.*, *Principles of Optics: Electromagnetic Theory of Propagation, Interference and Diffraction of Light*, 7th ed. Cambridge, U.K.: Cambridge Univ. Press, 1999.
[35] J. A. Nanzer, "Spatial filtering of grating lobes in mobile sparse arrays," in *Proc. IEEE Radio Wireless Symp. (RWS)*, Jan. 2016, pp. 26–28.
[36] P. Chatterjee and J. A. Nanzer, "Using platform motion for improved spatial filtering in distributed antenna arrays," in *Proc. IEEE Radio Wireless Symp. (RWS)*, Jan. 2018, pp. 253–255.
[37] P. C. Theofanopoulos, M. Sakr, and G. C. Trichopoulos, "Multistatic terahertz imaging using the radon transform," *IEEE Trans. Antennas Propag.*, vol. 67, no. 4, pp. 2700–2709, Apr. 2019.
[38] (2019). *Example SAR Data from ICEYE*. Accessed: Mar. 17, 2020. [Online]. Available: https://www.iceye.com/downloads/datasets
[39] A. Bovik, *The Essential Guide to Image Processing*. New York, NY, USA: Academic, 2009.
[40] C. Balanis, *Antenna Theory: Analysis and Design*. Hoboken, NJ, USA: Wiley, 2016.
[41] M. Haneishi, S. Yoshida, and M. Tabeta, "A design of back-feed type circularly polarized microstrip disk antennas having symmetrical perturbation element by one-point feed," *Electron. Commun. Jpn. I, Commun.*, vol. 64, no. 7, pp. 52–60, Jul. 1981. [Online]. Available: https://onlinelibrary.wiley.com/doi/abs/10.1002/ecja.4410640708
[42] S. M. Ellison, S. Mghabghab, J. J. Doroshewitz, and J. A. Nanzer, "Combined wireless ranging and frequency transfer for internode coordination in open-loop coherent distributed antenna arrays," *IEEE Trans. Microw. Theory Techn.*, vol. 68, no. 1, pp. 277–287, Jan. 2020.
[43] H. Ouassal, T. Rocco, M. Yan, and J. A. Nanzer, "Decentralized frequency synchronization in distributed antenna arrays with quantized frequency states and directed communications," *IEEE Trans. Antennas Propag.*, vol. 68, no. 7, pp. 5280–5288, Jul. 2020.
[44] S. M. Ellison and J. A. Nanzer, "High-accuracy multinode ranging for coherent distributed antenna arrays," *IEEE Trans. Aerosp. Electron. Syst.*, vol. 56, no. 5, pp. 4056–4066, Oct. 2020.
[45] P. Knott, "Design and experimental results of a spherical antenna array for a conformal array demonstrator," in *Proc. 2nd Int. ITG Conf. Antennas*, Mar. 2007, pp. 120–123.
[46] G. S. Karthikeya, N. Agnihotri, S. S. Siddiq, K. S. Mehul, and T. Thyagaraj, "A conformal UHF antenna for cargo helicopter belly," in *Proc. IEEE 5th Asia–Pacific Conf. Antennas Propag. (APCAP)*, Jul. 2016, pp. 285–286.
[47] S. P. Singh, A. Kumar, V. K. Singh, and Sagar, "A broadband wide beamwidth circulary polarized microstrip patch antenna with conformal radome for high-speed airborne communication," in *Proc. Int. Conf. Innov. Electron., Signal Process. Commun. (IESC)*, Apr. 2017, pp. 155–158.
[48] P. G. Fahlstrom and T. J. Gleason, *Introduction to UAV Systems*. Hoboken, NJ, USA: Wiley, 2012.
[49] (2017). *StarLite-2A Autonomous UAV Helicopter*. Accessed: Jun. 16, 2020. [Online]. Available: http://fettersaerospace.com/uav-helicopters.html
[50] T. Fawcett, "An introduction to ROC analysis," *Pattern Recognit. Lett.*, vol. 27, no. 8, pp. 861–874, Jun. 2006. [Online]. Available: http://www.sciencedirect.com/science/article/pii/S016786550500303X
[51] D. G. Altman and J. M. Bland, "Statistics notes: Diagnostic tests 2: Predictive values," *Brit. Med. J.*, vol. 309, no. 6947, p. 102, 1994. [Online]. Available: https://www.bmj.com/content/309/6947/102.1
[52] N. Metropolis and S. Ulam, "The Monte Carlo method," *J. Amer. Statist. Assoc.*, vol. 44, no. 247, pp. 335–341, 1949. [Online]. Available: http://www.jstor.org/stable/2280232

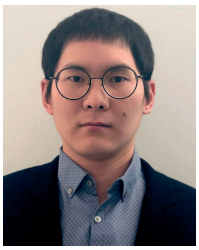

Daniel Chen (Graduate Student Member, IEEE) received the B.S. degree in electrical engineering from Michigan State University, East Lansing, MI, USA, in 2015, where he is currently pursuing the Ph.D. degree in electrical and computer engineering.

His current research interests include wireless microwave and millimeter-wave systems, antenna arrays, radars and signal processing.

Stavros Vakalis (Graduate Student Member, IEEE) received the diploma degree in electrical and computer engineering from the National Technical University of Athens, Athens, Greece in 2017, and the M.S. degree in electrical and computer engineering from Michigan State University, East Lansing, MI, USA, in 2020, where he is currently pursuing the Ph.D. degree in electrical engineering.

His current research interests include wireless microwave and millimeter-wave systems, millimeter-wave imaging, antenna arrays, radar and signal processing.

Mr. Vakalis is a member of the IEEE Microwave Theory and Techniques Society and the IEEE Antennas and Propagation Society. He has received for his graduate studies the Gerondelis Foundation Graduate Scholarship in 2019 and the IEEE Microwave Theory and Techniques Society (IEEE MTT-S) Graduate Fellowship Award in 2021. He was the recipient of the Second Place Awards of both the Student Paper Competition and the Student Design Competition at the 2020 IEEE International Symposium on Antennas and Propagation. He is currently serving as a Reviewer for the IEEE TRANSACTIONS ON MICROWAVE THEORY AND TECHNIQUES, the IEEE JOURNAL OF ELECTROMAGNETICS, RF AND MICROWAVES IN MEDICINE AND BIOLOGY, the IEEE TRANSACTIONS ON ANTENNAS AND PROPAGATION, and IEEE GEOSCIENCE AND REMOTE SENSING LETTERS.

Jeffrey A. Nanzer (Senior Member, IEEE) received the B.S. degree in electrical engineering and the B.S. degree in computer engineering from Michigan State University, East Lansing, MI, USA, in 2003, and the M.S. and Ph.D. degrees in electrical engineering from The University of Texas at Austin, Austin, TX, USA, in 2005 and 2008, respectively.

From 2008 to 2009, he was a Post-Doctoral Fellow with Applied Research Laboratories, the University of Texas at Austin, where he was involved in designing electrically small HF antennas and communication systems. From 2009 to 2016, he was with The Johns Hopkins University Applied Physics Laboratory, Laurel, MD, USA, where he created and led the Advanced Microwave and Millimeter-Wave Technology Section. In 2016, he joined the Department of Electrical and Computer Engineering, Michigan State University, where he is currently a Dennis P. Nyquist Assistant Professor. He has authored or coauthored more than 100 refereed journal and conference articles, authored *Microwave and Millimeter-Wave Remote Sensing for Security Applications* (Artech House, 2012), and coauthored the chapter*Photonics-Enabled Millimeter-Wave Wireless Systems* in wireless transceiver circuits (Taylor & Francis, 2015). His current research interests include distributed arrays, radar and remote sensing, antennas, electromagnetics, and microwave photonics.

Dr. Nanzer is a member of the IEEE Antennas and Propagation Society Education Committee and the USNC/URSI Commission B. He was a Founding Member and the First Treasurer of the IEEE APS/ MTT-S Central Texas Chapter. He served as the Vice-Chair for the IEEE Antenna Standards Committee from 2013 to 2015. He was the Chair of the Microwave Systems Technical Committee (MTT-16) and the IEEE Microwave Theory and Techniques Society from 2016 to 2018. He was a recipient of the Outstanding Young Engineer Award from the IEEE Microwave Theory and Techniques Society in 2019, the DARPA Director's Fellowship in 2019, the National Science Foundation (NSF) CAREER Award in 2018, the DARPA Young Faculty Award in 2017, and the JHU/APL Outstanding Professional Book Award in 2012. He is currently an Associate Editor of the IEEE TRANSACTIONS ON ANTENNAS AND PROPAGATION.